Modeling analysis of the influence of plasticity on high pressure deformation of hcp-Co

Sébastien Merkel[*]

Laboratoire de Structure et Propriétés de l'Etat Solide, CNRS, Université des Sciences et Technologies de Lille,
59655 Villeneuve d'Ascq, France

Carlos Tomé

MST Division, Los Alamos National Laboratory, Los Alamos, New Mexico 87545, USA

Hans-Rudolf Wenk

Department of Earth and Planetary Science, University of California-Berkeley, Berkeley, California 94720, USA
(Received 8 September 2008; published 18 February 2009)

Previously measured *in situ* x-ray diffraction is used to assess the development of internal elastic strains within grains of a sample of polycrystalline cobalt plastically deformed up to a pressure of 42.6 GPa. An elastoplastic self-consistent polycrystal model is used to simulate the macroscopic flow curves and internal strain development within the sample. Input parameters are single-crystal elastic moduli and their pressure dependence, critical resolved shear stresses, and hardening behavior of the slip and twinning mechanisms which are active in Co crystals. At 42 GPa, the differential stress in hcp-Co is 1.9 ± 0.1 GPa. The comparison between experimental and predicted data leads us to conclude that: (a) plastic relaxation plays a primary role in controlling the evolution and ordering of the lattice strains; (b) the plastic behavior of hcp-Co deforming under high pressure is controlled by basal and prismatic slip of $\langle a \rangle$ dislocations, and either pyramidal slip of $\langle c+a \rangle$ dislocations, or compressive twinning, or both. Basal slip is by far the easiest and most active deformation mechanism. Elastoplastic self-consistent models are shown to overcome the limitations of models based on continuum elasticity theory for the interpretation of x-ray diffraction data measured on stressed samples. They should be used for the interpretation of these experiments.

PACS number(s): 62.50.−p, 62.20.−x, 91.60.−x, 61.05.cp

I. INTRODUCTION

Characterizing the effect of pressure on elastic and plastic properties of condensed matter is particularly important for understanding elasticity, mechanical stability of solids, material strength, interatomic interactions, and phase-transition mechanisms. In particular, hexagonal-closed-packed (hcp) metals are of great interest because they tend to exhibit intriguing physical properties[1–4] that represent a challenge for first-principles calculations,[5–8] and also because the Earth's inner core could be mainly composed of the hcp polymorph of Fe, ϵ-Fe.[9]

In the past few years, techniques have been developed to study the plastic properties of materials *in situ* under combined high pressure and high temperature.[10–13] In those experiments x-ray diffraction is used to probe stress and lattice preferred orientations (LPOs) within the sample and extract physical properties such as dominant deformation mechanisms, flow laws, or ultimate stress. However, the theory commonly used for relating the measured lattice strains to stress and elastic properties[14] is based on lower or upper bound assumptions and has shown severe limitations. In particular, it was shown that this model yields inconsistent results for inverting single-crystal elastic properties for ϵ-Fe.[15–18] This was also confirmed by extensive work on hcp-Co which demonstrated that the method provides elastic moduli that are inconsistent with those provided by a range of other experimental and theoretical techniques.[3,5,19–23]

In the material science community, the issue of stress measurement using x-ray or neutron diffraction is known as residual stress analysis.[24,25] There is a body of work showing that the analysis of such data is not straightforward.[26–30] Indeed, stress and strain are very heterogeneous in plastically deformed materials and upper or lower bound models based on continuum elasticity theory do not account for this phenomenon. Various techniques have been developed for the interpretation of experimental data, based on self-consistent methods,[26,31] or finite-element modeling.[28] Self-consistent analysis has already been applied to high pressure solids with a cubic structure[32,33] and to trigonal quartz.[34]

Here, we look at the plastic properties of hcp Co under pressure. Cobalt lies next to iron in the Periodic Table and its hcp phase has a wide stability field.[35] Unlike the hcp phase of iron, it is stable at ambient pressure with readily available single crystals. As such, it has become a paradigm for comparing and testing numerous high pressure techniques. The phase diagram and equation of state have been studied using both x-ray diffraction[35–37] and first-principles calculations.[5,8] Elastic properties have been obtained under ambient pressure using ultrasonic techniques[38] and at high pressure using inelastic x-ray scattering[19,20,39] (IXS), Raman spectroscopy,[3] impulsive stimulated light scattering,[23] and first-principles techniques.[5] The plastic properties of hcp-Co have been investigated under ambient pressure for both coarse grains[40–44] and nanocrystalline samples.[45–47] High pressure diamond-anvil cell (DAC) radial diffraction (RDX) experiments have been reported,[22] but lacked an interpretation based on the interplay between elastic and plastic mechanisms.

In this paper, we use a modification of the elastoplastic self-consistent (EPSC) model of Turner and Tomé[31] to simulate and interpret DAC experiment previously done on a Co aggregate for pressures up to 42.6 GPa.[22] This model yields information about the absolute strength of the deformation mechanisms involved, stress distribution among grains in the
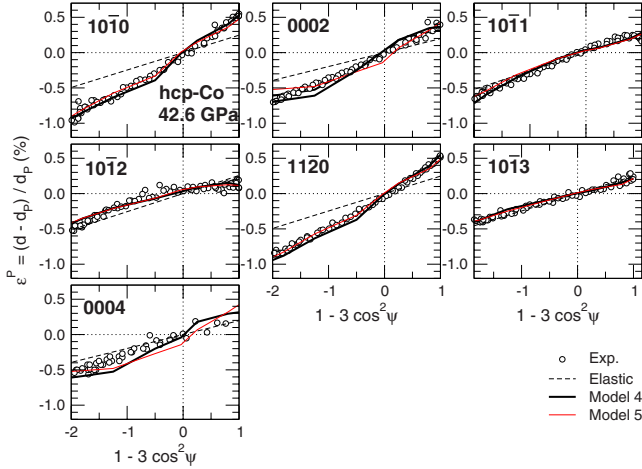
FIG. 1. (Color online) Measured and simulated strains vs $(1-3\cos^2\psi)$ under the hydrostatic pressure of 42.6 GPa. Circles are data from Ref. 22. d are measured d spacings and d_P d spacings under equivalent hydrostatic pressure. Thick black lines are results of EPSC calculations using model 4 in Table II. Thin red lines are results of EPSC calculations using model 5 in Table II. Thin dashed lines are predictions of an elastic model with no effect of LPO (Ref. 14) assuming a differential stress of 4 GPa. In all cases, the d spacings under equivalent hydrostatic pressure d_P have been obtained assuming relation 15.
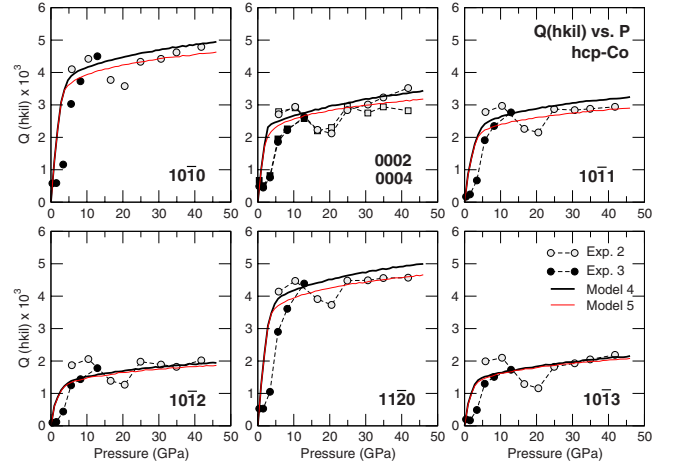

FIG. 2. (Color online) Measured and simulated lattice strain parameters vs pressure for the $10\bar{1}0$, 0002, 0004, $10\bar{1}1$, $10\bar{1}2$, $11\bar{2}0$, and $10\bar{1}3$ diffraction lines of hcp-Co. Gray symbols are data from Exp. 2 in Ref. 22, solid symbols are data from Exp. 3 in Ref. 22, thick black lines are EPSC simulations using model 4 in Table II, and thin red lines are EPSC simulations using model 5 in Table II. Experimental data for the 0004 diffraction line are shown using square symbols. All other experimental data are represented with circles.

sample, and true stress values for the polycrystal. In addition, our modeling shows the important role that plastic relaxation and nonhomogeneity of stress and strain play in high pressure experiments.

II. METHODS

A. Experimental data

The experimental data on hcp-Co that we use here have been published previously.[22] Two experiments were performed in which a sample of pure hcp-Co was compressed in a diamond-anvil cell, up to 42.6 GPa for the first run and up to 12.8 GPa for the second run. Diffraction data were collected in a radial geometry with the incoming x-ray beam perpendicular to the load axis.

Figure 1 shows measured strains for several crystallographic planes vs $(1-3\cos^2\psi)$ for a hydrostatic pressure of 42.6 GPa, where ψ is the angle between the diffracting plane normal and the direction of maximum stress. They are nearly linear with $(1-3\cos^2\psi)$, as predicted by purely elastic lattice strain theory.[14] However, it was shown that stresses calculated using this theory for individual lattice planes were inconsistent.[22]

For all pressures in the experiment, the variations in diffraction intensity with orientation were used to extract lattice preferred orientations in the sample, while peak shifts were used to extract lattice strains parameters Q (discussed in Sec. II B 4) for the $10\bar{1}0$, 0002, $10\bar{1}1$, $10\bar{1}2$, $11\bar{2}0$, $10\bar{1}3$, and 0004 diffraction lines of hcp-Co (Fig. 2).

B. Elastic model

1. Stress and strain

Under high pressure, it is preferable to separate the effect of hydrostatic pressure and deviatoric stress, and define elastic moduli as relating stress and strain deviations relative to the hydrostatic state. Elastic constants are then appropriate for calculation of elastic wave velocities and comparison with previous work. This relation is not trivial under pressure,[48–50] and we therefore discuss several definitions of stress and strains. In this paper, the superscript "0" will refer to absolute stress and strain (relative to ambient pressure), while the superscript "P" will refer to stress, strain, or stiffness relative to the state of hydrostatic pressure P.

The relation between stress tensors relative to ambient pressure (absolute stress) σ_{ij}^0 and stress tensors relative to the hydrostatic pressure (relative stress) σ_{ij}^P is straightforward,

$$\sigma_{ij}^0 = \sigma_{ij}^P + P \cdot \delta_{ij} = C_{ijkl}^P \epsilon_{kl}^P + P \cdot \delta_{ij}, \tag{1}$$

where δ_{ij} is the Kronecker function and ϵ_{ij}^P the strain tensor relative to the state of hydrostatic pressure. σ_{ij}^P is often referred to as deviatoric stress in the literature, although it may not be traceless at the grain level. C_{ijkl}^P are single-crystal elastic moduli for a medium under hydrostatic pressure P.

Strain definitions can be more complicated. If we consider an element of length d_0 under ambient pressure, length d_P at the hydrostatic pressure P, and length d under a general stress σ_{ij}^0, we define the following lattice strains:

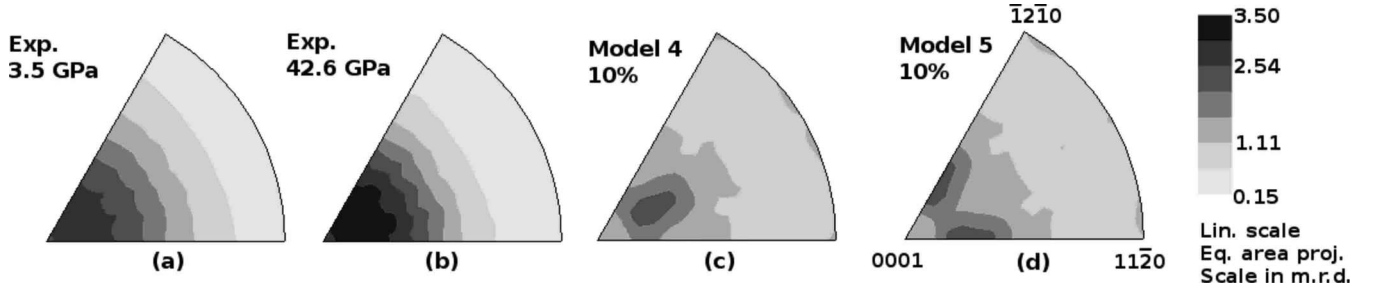$$\epsilon^P = \frac{d - d_P}{d_P}, \tag{2}$$

FIG. 3. [(a) and (b)] Experimental and [(c) and (d)] simulated inverse pole figures of the compression direction for hcp-Co. [(a) and (b)] Experimental data are from Exp. 2 in Ref. 22. Simulations are results of VPSC calculations using models (c) 4 and (d) 5 in Table II after 10% strain. Equal area projection, linear scale, and contours in m.r.d.

$$\epsilon^0 = \frac{d - d_0}{d_0}, \qquad (3)$$

$$\epsilon_P^0 = \frac{d_P - d_0}{d_0}, \qquad (4)$$

from where

$$\epsilon^0 = (1 + \epsilon_P^0)\epsilon^P + \epsilon_P^0. \qquad (5)$$

ϵ^P are the strains relative to the hydrostatic pressure state and could be referred to as "relative strains;" ϵ^0 are the strains relative to the ambient pressure state and could be referred to as "absolute strains."

Note that elastic moduli under hydrostatic pressure C_{ijkl}^P relate relative strains ϵ_{ij}^P and relative stresses σ_{ij}^P, and that the relation between absolute strains ϵ_{ij}^0 and absolute stresses σ_{ij}^0 is not straightforward.

2. Coordinate systems

Analysis and calculations can be simplified if single-crystal elastic moduli, d spacings measured using x-ray diffraction, and sample stress, are expressed in the suitable coordinate system.

The diamond-anvil cell geometry defines a sample coordinate system, K_S, with $\mathbf{Z}_S$ aligned with the compression direction and $\mathbf{Y}_S$ parallel to the incoming x-ray beam, pointing toward the detector. This coordinate system is well defined in the experiment and useful to relate all information expressed in the other systems. Stress in diamond-anvil cells are mostly axial and, when expressed in K_S, the stress applied to the polycrystalline sample reads

$$\sigma^{P-K_S} = \begin{bmatrix} -\frac{t}{3} & 0 & 0 \\ 0 & -\frac{t}{3} & 0 \\ 0 & 0 & 2\frac{t}{3} \end{bmatrix}, \qquad (6)$$

where t is the differential stress.

The diffraction direction defines a diffraction coordinate system K_D with the axis $\mathbf{Z}_D$ parallel to the scattering vector $\mathbf{N}$ (bisector between the incoming beam and the diffracted x-ray beam collected by the detector) and $\mathbf{Y}_D$ perpendicular to $\mathbf{Z}_D$ and contained in the plane defined by the incident and diffracted beams. In K_D the d spacings measured in diffraction are the 33 component of the crystal strain tensor

$$\epsilon_{33}^{P-K_D} = \frac{d_m(hkl) - d_P(hkl)}{d_P(hkl)}, \qquad (7)$$

where $d_m(hkl)$ is the measured d spacing for the hkl reflection and $d_P(hkl)$ is the d spacing of the hkl reflection under the hydrostatic pressure P.

The crystal coordinate system K_C is defined by the (orthogonal) crystal axes. Microscopic physical relations, such as Hooke's law relating the microscopic stress, strain, and single-crystal elastic moduli refer to each crystallite coordinate system K_C. d spacings for hkl reflections in individual grains should be extracted from calculations using Hooke's law in K_C.

3. Texture and lattice preferred orientations

The texture in the sample can be represented by an orientation distribution function (ODF). The ODF is required to estimate anisotropic physical properties of polycrystals such as elasticity or plasticity.[51] The ODF represents the probability for finding a crystal orientation, and it is normalized such that an aggregate with a random orientation distribution has a probability of one for all orientations. If preferred orientation (texture) is present, some orientations have probabilities higher than one and others lower than one.

The ODF can be calculated using the variation in diffraction intensity with orientation using tomographic algorithms such as WIMV,[52] as implemented in the BEARTEX package[53] or in the "Maud Rietveld" refinement program.[54] This technique has been successfully applied to measure textures and deduce active high pressure deformation mechanisms.[55]

Textures of the sample analyzed here have been described in detail[22] and Fig. 3 presents inverse pole figures of the compression direction for experiment 2 at 3.5 and 42.6 GPa. For hcp-Co compressed in the DAC, we observe the development of a relatively strong texture with a maximum at about 15° from 0001.

4. Elastic strains

For polycrystals, diffraction peaks are the sum of the contribution from all crystallites in the correct reflection conditions, i.e., crystallites whose normal to the (hkl) plane is parallel to the scattering vector $\mathbf{N}$. The corresponding individual d spacings depend on the local stress and elastic properties in the grain considered. The measured d spacing

$d_m(hkl)$ is a weighted arithmetic mean of those individual d spacings and corresponds to the 33 component of the elastic strain tensor in the diffraction coordinate system, K_D [Eq. (7)].

Theories have been developed to relate single-crystal elastic moduli to measured d spacings for stressed polycrystals. Most models rely on elasticity theory and assume either continuity of stress or of strain within the sample. If, in addition, it is assumed that the sample is nontextured, it can be shown that the lattice strain can be expressed as[14]

$$\epsilon_{33}^{P-K_D} = \frac{d_m(hkl) - d_P(hkl)}{d_P(hkl)} = Q(hkl)(1 - 3\cos^2\psi), \quad (8)$$

where ψ is the angle between the diffracting plane normal and the maximum stress direction ($\mathbf{Z}_S$ in our case), and the lattice strain parameter $Q(hkl)$ is a function of the differential stress t in the polycrystal and single-crystal elastic moduli C_{ijkl}^P.

Theories that include texture effects have also been developed.[56] In this case, the measured d spacings do not vary linearly with $(1 - 3\cos^2\psi)$ but can still be related to differential stress in the polycrystal and single-crystal elastic moduli. However, deviations between predictions of theories that include texture effects and those that neglect it are small and may be difficult to separate experimentally.[57] In any case, it has been shown that this theory does not apply to data measured on materials where plastic deformation takes place. In particular, these techniques yield inconsistent stresses and elastic constants for hcp-Co under pressure.[21,22,58]

C. Plastic model

1. EPSC model

The evolution of stress and strain with deformation observed in Co can be related to results of ambient pressure experiments on other hcp metals (i.e., Be, Mg, and Ti) undergoing plastic deformation which show a similar behavior.[27,29,59,60] hkl-dependent stresses deduced from lattice strains have already been documented and modeled for fcc metals and ionic solids with the NaCl structure using EPSC simulations.[26,32,33] In those simulations, certain hkl reflections show a behavior close to that of a pure elastic deformation, while others do not, displaying either larger or smaller effective stresses.

The EPSC model we use here[31] represents the aggregate by a discrete number of orientations with associated volume fractions. The latter are chosen such as to reproduce the initial texture of the aggregate. EPSC treats each grain as an ellipsoidal elastoplastic inclusion embedded within a homogeneous elastoplastic effective medium with anisotropic properties characteristic of the textured aggregate. The external boundary conditions (stress and strain) are fulfilled on average by the elastic and plastic deformations at the grain level. The self-consistent approach explicitly captures the fact that soft-oriented grains tend to yield at lower stresses and transfer load to plastically hard-oriented grains, which remain elastic up to rather large stress.

The model uses known values of single-crystal elastic moduli. The parameters associated with each plastic deformation mode are the critical resolved shear stresses (CRSS), given by a hardening evolution law. The simulated internal strains are compared to experimental data by identifying the grain orientations which, in the model aggregate, contribute to the experimental signal associated with each diffracting vector.

An EPSC simulation is based on applying stress or strain increments to the aggregate, depending on the boundary conditions, until the final deformation or stress state is achieved. At each step, stress and strain in each grain are incremented accordingly, as follows from its interaction with the effective medium representing the aggregate. The response of medium and grain is assumed to be described by a linear relation between stress and total strain increments,

$$\delta\sigma^c = L^c : \delta\epsilon^{c,\text{total}}, \quad (9)$$

$$\delta\bar{\sigma} = \bar{L} : \delta\bar{\epsilon}^{\text{total}}, \quad (10)$$

$$\delta\epsilon^{\text{total}} = \delta\epsilon^{\text{elastic}} + \delta\epsilon^{\text{plastic}}. \quad (11)$$

Here $\bar{L}$ is the elastoplastic stiffness of the aggregate and $L^c = C^c : (I - \Sigma_s m^s \otimes f^s)$ is the elastoplastic stiffness of the crystal. C^c is the single-crystal elastic tensor, and the sum is taken over the active slip systems s in the grain. m^s is the Schmid tensor which resolves the shear component of the stress or strain along a slip system and f^s is a tensor which relates stress and strain rates.[61,62] As more systems become plastically active, the moduli L^C become more compliant. The stress equilibrium condition is solved for each grain assuming an ellipsoidal grain shape and using the Eshelby inclusion formalism. This procedure provides for a stress and strain increment in each grain. The macroscopic elastoplastic stiffness $\bar{L}$ is derived iteratively by enforcing the condition that the polycrystal response has to be given by the weighted average of the individual grains responses and has to be consistent with the boundary conditions.[31] The main advantage of the EPSC model is that it allows for grains to deform more or less than the average, depending on their degree of hardening, their orientation, and their relative directional stiffness with respect to the medium.

2. Parameters and output of EPSC models

In our modeling of DAC RDX data, we assume that the sample was submitted to an axial compression along $\mathbf{Z}_S$ in K_S. In all simulations, we assume that the sample consists of 1000 randomly oriented spherical grains, with single-crystal elastic moduli and their pressure dependence taken from IXS measurements[19] (Table I). The polycrystalline sample is

TABLE I. Ambient pressure and first pressure derivative of elastic moduli of hcp-Co measured using IXS between 0 and 39 GPa (Ref. 19). In our simulation $C_{ij}^P = C_{ij}^0 + P \cdot (\partial C_{ij}/\partial P)$.

	C_{11}	C_{33}	C_{12}	C_{13}	C_{44}
C_{ij}^0 (GPa)	293	339	143	90	78
$\partial C_{ij}/\partial P$	6.1	7.6	3.0	4.2	1.38

compressed in 3000 strain steps to a final state of strain defined by

$$\epsilon_x^{0-K_S} = -0.01$$

$$\epsilon_y^{0-K_S} = -0.01 \tag{12}$$

$$\epsilon_z^{0-K_S} = -0.17,$$

where strains are expressed in K_S relative to dimensions under ambient pressure. The deformation geometry was derived from x-ray radiographs of the sample taken during the DAC experiments[63] which indicate that our sample was submitted to very little radial deformation. The final value of the axial component $\epsilon_z^{0-K_S}$ was chosen to match the simulated and experimental pressures at the end of the compression.

The model uses combinations of seven deformation mechanisms typically found in hexagonal metals: slip of $\frac{1}{3}\langle 11\bar{2}0 \rangle$, or $\langle a \rangle$ dislocations, on basal (0001), prismatic $\{10\bar{1}0\}$, and pyramidal $\{10\bar{1}1\}$ planes; slip of $\frac{1}{3}\langle 11\bar{2}3 \rangle$, or $\langle c+a \rangle$ dislocations, on pyramidal $\{10\bar{1}1\}$ or $\{11\bar{2}2\}$ planes; tensile twinning on $\{10\bar{1}2\}$ planes; and, finally, compressive twinning on $\{11\bar{2}2\}$ planes (Table II). For each slip and twin mode we describe the hardening of CRSS by means of an empirical Voce hardening rule

$$\tau = \tau_0 + (\tau_1 + \theta_1 \Gamma)\left\{1 - \exp\left(-\frac{\theta_0 \Gamma}{\tau_1}\right)\right\}, \tag{13}$$

where τ is the instantaneous CRSS of the mechanism, τ_0 and $\tau_0 + \tau_1$ are the initial and final back-extrapolated CRSS, respectively, θ_0 and θ_1 are the initial and asymptotic hardening rates, and Γ is the accumulated plastic shear strain in the

grain. Strain levels presented here are relatively low, so we reduced the number of adjustable parameters by assuming that $\tau_1 = 0$. In this case, the hardening law becomes linear according to

$$\tau = \tau_0 + \theta_1 \Gamma, \tag{14}$$

and only two adjustable parameters remain.

Output of the simulation includes the relative activity of the various deformation mechanisms, the average stress in the polycrystal, stress and strain within each grain of the sample, and predicted lattice strains. The simulated elastic lattice strains were compared to experimental data by identifying the model grains whose crystallographic planes are oriented such as to contribute to the experimental signal. The lattice strain (peak shift) is calculated as a weighted average over all grains that contribute to the peak. Specifically, we considered $10\bar{1}0$, 0002, $10\bar{1}1$, $10\bar{1}2$, $11\bar{2}0$, and $10\bar{1}3$ diffraction lines at $\psi = 0$, $15°$, $30°$, $45°$, $60°$, $75°$, and $90°$. The region of orientation space which contributes to the signal was assumed to be within an interval of $\pm 7.5°$ with respect to the diffraction vector.

3. Representation of simulated and experimental data

It has been shown that Eq. (8) does not apply to data collected in RDX when samples are plastically deformed. However, previous RDX experiments[4,12,15,64–67] have shown that the measured d spacings are nearly linear when plotted vs $(1 - 3\cos^2 \psi)$ and that the d spacings measured for $\psi = 54.7°$ do correspond to those expected under the hydrostatic equivalent pressure. Therefore, experimental data were reduced using

TABLE II. List of deformation mechanisms used in the simulations. τ_0 and θ_1 are parameters for the simplified Voce hardening rule Eq. (14) and are expressed in GPa. Stars indicate deformation mechanisms that were not included in the final model.

Mechanism		Model 1		Model 2		Model 3		Model 4		Model 5	
		τ_0	θ_1	τ_0	θ_1	τ_0	θ_1	τ_0	θ_1	τ_0	θ_1
Basal	$(0001)\langle\bar{1}2\bar{1}0\rangle$	100	1	1	1	8	1	0.07	0.30	0.07	0.30
Prismatic	$\{10\bar{1}0\}\langle\bar{1}2\bar{1}0\rangle$	100	1	8	1	1	1	0.90	1.00	0.90	1.00
Pyramidal $\langle a \rangle$	$\{10\bar{1}1\}\langle\bar{1}2\bar{1}0\rangle$	100	1	100	1	100	1	*	*	*	*
Pyramidal $\langle c+a \rangle$	$\{10\bar{1}1\}\langle11\bar{2}3\rangle$	100	1	100	1	100	1	0.70	1.50	*	*
Pyramidal $\langle c+a \rangle$ second order	$\{11\bar{2}2\}\langle11\bar{2}3\rangle$	*	*	*	*	*	*	*	*	*	*
Tensile twin	$\{10\bar{1}2\}\langle10\bar{1}1\rangle$	*	*	*	*	*	*	*	*	*	*
Compressive twin	$\{2\bar{1}\bar{1}2\}\langle2\bar{1}\bar{1}3\rangle$	*	*	*	*	*	*	*	*	0.60	0.70

$$\epsilon_{33}^{P-K_D}(hkil, \psi) = \frac{d_m(hkil, \psi) - d_P(hkil)}{d_P(hkil)}$$

$$= Q(hkil)(1 - 3\cos^2\psi), \qquad (15)$$

where $d_m(hkil, \psi)$ is the measured d spacing for the $hkil$ diffracting line at angle ψ, $d_P(hkil)$ is the d spacing for the $hkil$ line under hydrostatic pressure P, and $Q(hkil)$ is the lattice strain parameter for the $hkil$ line. $d_P(hkil)$ and $Q(hkil)$ were adjusted to the experimental data. $d_P(hkil)$ was then used to estimate the average lattice parameters a and c of the hexagonal crystal and the hydrostatic pressure P using a known equation of state.[36] Experimental data for hcp-Co lattice strains vs pressure obtained using such procedure are extracted from Ref. [22] and summarized in Fig. [2].

The EPSC model calculates the average stress in the sample, σ^{0-K_S}, from which we deduce the hydrostatic pressure and differential stress

$$P = (\sigma_{11}^{0-K_S} + \sigma_{22}^{0-K_S} + \sigma_{33}^{0-K_S})/3, \qquad (16)$$

$$t = \sigma_{33}^{0-K_S} - \left(\frac{\sigma_{11}^{0-K_S} + \sigma_{22}^{0-K_S}}{2}\right), \qquad (17)$$

respectively. The EPSC model also provides absolute simulated strains $\epsilon_{33}^{0-K_D}(hkil, \psi)$ relative to d spacings under ambient pressure, which were used to calculate strains induced by the hydrostatic pressure, ϵ_P^0, and deviatoric lattice strains parameters $Q(hkil)$. The procedure consists in fitting a and b parameters to

$$\epsilon_{33}^{0-K_D}(hkil, \psi) = \frac{d_m(hkil, \psi) - d_0(hkil)}{d_0(hkil)} = a + b(1 - 3\cos^2\psi). \qquad (18)$$

Using Eqs. [5] and [15], we get

$$\epsilon_P^0 = \frac{d_P(hkil) - d_0(hkil)}{d_0(hkil)} = a, \qquad (19)$$

$$Q(hkil) = \frac{b}{1+a}. \qquad (20)$$

4. Pressure dependence of the elastic moduli

Since the original EPSC code did not include the effect of pressure on elastic moduli, we modified it to calculate pressure and update the corresponding elastic moduli, at each step and in each grain. At each step i, the elastic strain increment induced by the increment of stress applied to a grain is calculated using

$$\delta\epsilon_{kl}^{P-K_C}|_i = S_{klmn}^P[\sigma_{mn}^{0-K_C}|_i - \sigma_{mn}^{0-K_C}|_{i-1}], \qquad (21)$$

where the coefficients S_{klmn}^P are elastic compliances, function of the hydrostatic pressure in the grain at step $(i-1)$, and stress tensors are absolute, relative to the state under ambient pressure. Lattice spacing for each grain contributing to the diffraction peak is then updated using

$$d(hkil)|_i = d(hkil)|_{i-1}(1 + \delta\epsilon_{33}^{P-K_D}), \qquad (22)$$

where $\delta\epsilon_{33}^{P-K_D}$ is the component of the strain tensor $\delta\epsilon_{kl}^{P-K_C}$ perpendicular to the diffracting plane.

The average lattice strain for each reflection and orientation to be compared with experimental data is then updated by identifying the grains contributing to the diffraction and calculating

$$\epsilon^0(hkil) = \left[\frac{d(hkil)|_i - d(hkil)|_0}{d(hkil)|_0}\right], \qquad (23)$$

where the average is taken over all grains contributing to the diffraction.

III. RESULTS

In this section, we present simulations of the DAC experiment done for hcp-Co using the EPSC model. In order to study the effect of plasticity upon the lattice strain evolution, we consider several combinations of active slip and twinning modes, and several combinations of hardening parameters. We will refer to each of these combinations as a crystal model. The different sets and associated hardening parameters are listed in Table [II]. In all cases, we use the pressure dependent elastic moduli for Co listed in Table [I].

A. Pressure dependence of elastic moduli and hydrostatic equation of state

According to the elastic theory introduced earlier, d spacings measured at $\psi = 54.7°$ correspond to those associated with the hydrostatic pressure P [see Eq. [15]]. While the theory used to derive this result has strong limitations, numerous RDX experiments have shown that equation of states measured at this angle tend to correspond to those measured under hydrostatic conditions.

Figure [4] presents the pressure dependence of $\epsilon_P^0 = (d_P - d_0)/d_0$ simulated with the EPSC model along with results from RDX (Ref. [22]) at $\psi = 54.7°$. The figure also shows curves calculated using the bulk modulus and pressure dependence of the c/a ratio measured under hydrostatic conditions[36] as well as compression curves calculated using the single-crystal elastic moduli and their pressure dependence measured using IXS (Ref. [19]) that were assumed in the calculation.

Compression curve calculated using the single-crystal elastic moduli and their pressure dependence measured using IXS differ slightly from those measured under hydrostatic conditions. RDX results almost coincide with those deduced from the hydrostatic equation of state, while EPSC results almost coincide with those deduced from IXS measurements. Small differences can be seen for $10\bar{1}3$ and 0002 and they will be discussed later. It is obvious from Fig. [4] how critical it is, in this simulation, to account for the pressure dependence of the elastic constants. Otherwise, predictions tend to grossly overestimate the lattice strains as a function of pressure.
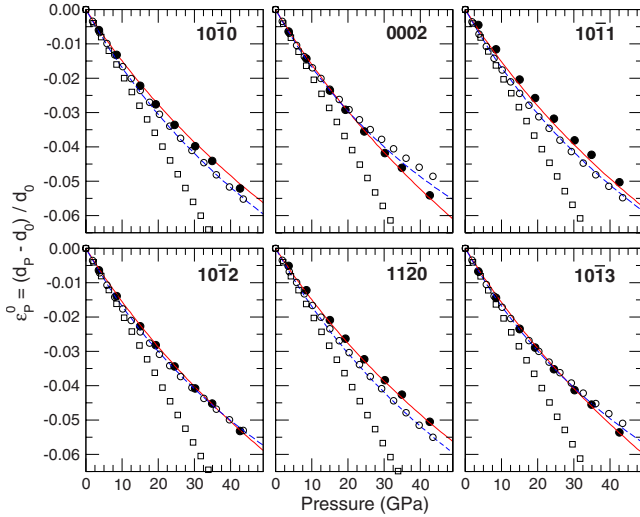
FIG. 4. (Color online) Measurement of hydrostatic strain vs pressure. Solid line is deduced from an equation of state measured under hydrostatic conditions (Ref. 36), dashed lines is deduced from the single-crystal elastic moduli measured using IXS (Ref. 19), black circles are measurement from radial x-ray diffraction (Ref. 22) at $\psi = 54.7°$, open squares are simulated using EPSC and no pressure dependence of elastic moduli, and open circles are results of EPSC models using the elastic moduli and their pressure dependence measured using IXS (Ref. 19).

B. Effect of individual deformation mechanisms on the simulated lattice strains

Figure 5 presents the results of the EPSC calculations for plasticity models 1, 2, and 3 (Table II). For each, we show the evolution of the polycrystal stress components σ_{11} and σ_{33}, hydrostatic pressure P, differential stress t, the simulated deviatoric lattice strain parameter $Q(hkil)$, and the deformation mechanisms relative activity as a function of the applied axial strain $\epsilon_z^{0-K_S}$.

Pressure calculated as a function of $\epsilon_z^{0-K_S}$ is independent of the plasticity model used. For all cases, we obtain an evolution of pressure with $\epsilon_z^{0-K_S}$ compatible with predictions based on the hydrostatic equation of state of hcp-Co. At the end of our simulated compression, the sample volume is reduced by 17% and pressure is 46.2 GPa. As demonstrated in Fig. 5, all other results strongly depend on the plastic model and they should be discussed independently.

For model 1, the strength of all deformation mechanisms is purposely set too high for them to be activated. As a consequence, the behavior of the polycrystal is fully elastic. The differential stress and pressure in the sample increase continuously with applied strain and t reaches a value of 38.3 GPa at a pressure of 46.2 GPa. The simulated lattice strain parameters Q also increase continuously with pressure and are about 1 order of magnitude higher than those measured in the experiment [Figs. 2 and 5(c)].

In model 2, basal slip is activated when the applied strain reaches 0.0122. At this strain, pressure and differential stress in the sample are 2.2 and 2.1 GPa, respectively. The activation of basal slip is correlated with a drop in the simulated lattice strains for diffraction lines such as $10\bar{1}1$, $10\bar{1}2$, and

$10\bar{1}3$, corresponding to pyramidal planes, while lattice strains for lines such as $10\bar{1}0$, $11\bar{2}0$, and 0002, corresponding to basal and prismatic planes, remain largely unaffected. The activation of basal slip also coincides with a lower rate of increase in the differential stress. Prismatic slip is activated when $\epsilon_z^{0-K_S}$ reaches 0.1170, corresponding to a pressure and differential stress of 27.6 and 11.3 GPa, respectively. The activation of prismatic slip correlates with a second inflection in the evolution of t with strain. Activation of prismatic slip induces a drop in the simulated lattice strain for $10\bar{1}0$ and $11\bar{2}0$, while strains for lines corresponding to basal planes, such as 0002, remain largely unaffected. At the end of the compression, differential stress reaches a value of 14.2 GPa at a pressure of 46.2 GPa.

In model 3, prismatic slip is activated when $\epsilon_z^{0-K_S}$ reaches 0.0122. At this strain, pressure and differential stress in the sample are 2.2 and 2.1 GPa, respectively. The activation of prismatic slip is correlated with a drop in the simulated lattice strains for diffraction lines such as $10\bar{1}0$, $11\bar{2}0$, while simulated lattice strains for lines corresponding to pyramidal and basal planes remain largely unaffected. Basal slip is activated when $\epsilon_z^{0-K_S}$ reaches 0.1190, corresponding to a pressure and differential stress of 28.2 and 11.1 GPa, respectively. The activation of basal slip is correlated with a drop in the simulated lattice strains for the lines such as $10\bar{1}1$, $10\bar{1}2$, and $10\bar{1}3$, corresponding to pyramidal planes, while lattice strains for lines corresponding to basal planes remain largely unaffected. In all cases, activation of a plastic mode induces a decrease in slope for t vs applied strain. At the end of the compression, differential stress reaches a value of 13.7 GPa at a pressure of 46.2 GPa.

We conclude from the above results that basal and prismatic slips split the strain evolution of the different diffraction lines, but do not reproduce the observed experimental sequence. Also, basal activity relaxes strains in lines corresponding to pyramidal planes, and prism activity in lines corresponding to prismatic planes. In addition, although basal and prismatic slips lower the predicted lattice strains in comparison with the fully elastic model 1, they alone do not provide enough relaxation resulting in simulated strains larger than the measured ones. Since basal and prism slip do not provide deformation along the c axis of the Co crystal, we explore below the effect of the activation of crystallographic modes with a c-axis deformation component.

C. Optimized model

Models 4 and 5 (Table II) were found to best match the experimental data (Figs. 1, 2, and 6). Among the typical deformation mechanisms found in hcp metals, four were selected: basal, prismatic, and either pyramidal $\langle c+a \rangle$ slip or compressive twinning. For both models, initial CRSS τ_0 and hardening rate θ_1 were optimized to best match the measured lattice strains and their evolution with pressure. Other mechanisms, listed in Table II, were investigated but not included in the final model. For instance, pyramidal $\langle a \rangle$ slip lowers lattice strains parameters Q for most lines except $10\bar{1}3$ and 0002 and activation of tensile twinning separates
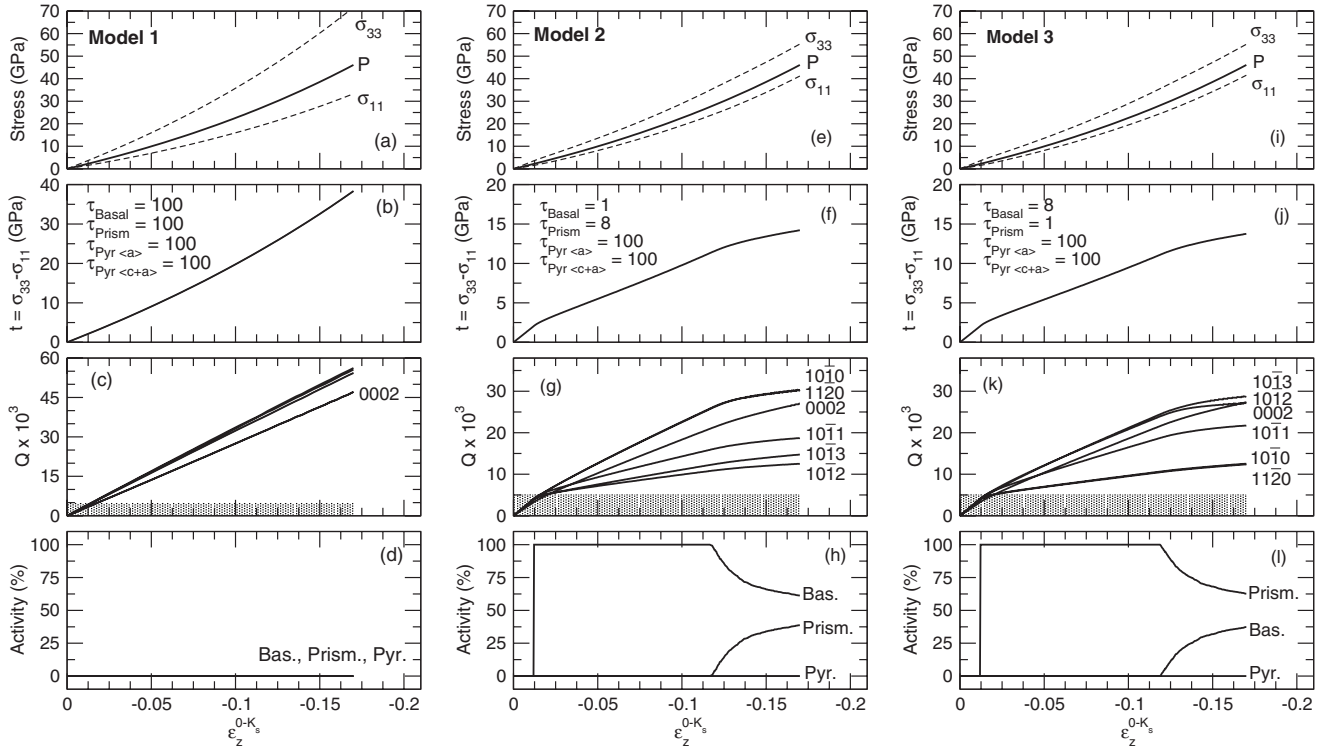
FIG. 5. σ_{11} and σ_{33} stress components, pressure [(a),(e),(i)], differential stress [(b),(f),(j)], lattice strain parameters [(c),(g),(k)], and relative activity of the deformation mechanisms [(d),(h),(l)], as a function of axial strain for simulations using models 1 [(a),(b),(c),(d)], 2 [(e),(f),(g),(h)], and 3 [(i),(j),(k),(l)] listed in Table II. In all cases, lattice strains simulated for the $10\bar{1}0$ and the $11\bar{2}0$ diffraction lines cannot be distinguished. For models 2 and 3 [Figs. 5(g) and 5(k)], Miller indices for which the lattice strains are calculated are labeled on the figure. For model 1, lattice strains for $10\bar{1}0$, $11\bar{2}0$, $10\bar{1}1$, $10\bar{1}2$, and $10\bar{1}3$ diffraction lines cannot be distinguished at this scale and are not labeled. Shaded area in Figs. 5(c), 5(g), and 5(k) indicates the order of magnitude of the experimental measurements. In all cases, pyramidal slip systems do not get activated. For model 1, none of the slip system gets activated and the simulation is fully elastic.

lattice strain parameters Q from $10\bar{1}0$ and $11\bar{2}0$; those effects cannot be reconciled with the measured data.

In both optimized models, the strength of basal slip mostly controls lattice strains simulated for $10\bar{1}1$, $10\bar{1}2$, and $10\bar{1}3$, while that of prismatic slip mostly influences $10\bar{1}0$ and $11\bar{2}0$ lattice strains. For model 4, 0002 lattice strains are controlled by pyramidal $\langle c+a \rangle$ slip, while in model 5, they are controlled by the activation of compressive twinning.

Basal slip is by far the easiest slip system with an initial CRSS of 0.07 GPa and a hardening coefficient of 0.3 GPa. In both models, the relative strength of prismatic slip and compressive twinning (model 5) or pyramidal slip (model 4) were adjusted to start prismatic slip last and eventually take over the deformation (Fig. 6). This was important to properly reproduce the measured 0002 lattice strains which are on the same order of magnitude that those of $10\bar{1}0$ and $11\bar{2}0$ early in the compression and saturate later on.

In model 4, basal slip is activated at $P=0.2$ GPa, with $t=0.2$ GPa. Pyramidal slip is activated when the pressure and differential stress are 2.3 and 1.0 GPa, respectively. Finally, prismatic slip is activated when $P=4.3$ GPa and $t=1.3$ GPa. At the end of the compression, the differential stress reaches 2.0 GPa at a pressure of 46.2 GPa.

In model 5, basal slip is activated at $P=0.2$ GPa, with $t=0.2$ GPa. Compressive twinning is activated when the

pressure and differential stress are 1.7 and 0.8 GPa, respectively. Finally, prismatic slip is activated when $P=2.8$ GPa and $t=1.0$ GPa. At the end of the compression, the differential stress reaches 1.8 GPa at a pressure of 46.2 GPa.

D. Plasticity and texture evolution

Slip and twinning induce grain reorientation and, as a consequence, texture evolution. In our experiments we start from a random aggregate of Co crystals and finish with a textured aggregate, where the c axis shows a tendency to align with the compression direction. This confirms that plastic deformation takes place during the DAC test. What remains to be tested is whether the experimental texture is consistent with compressive twinning or $\langle c+a \rangle$ slip activity, as models 4 and 5 predict, respectively.

The EPSC code that we use here does not account for grain reorientation associated with plastic deformation and cannot be used to simulate texture evolution. Similarly to our EPSC model, the viscoplastic self-consistent (VPSC) code[68] treats each grain as a viscoplastic inclusion in a homogeneous matrix that has the average properties of the polycrystal and can be used for texture simulations. Starting with an initial distribution of crystallite orientations and assuming deformation by slip and twinning, we can simulate a deformation path by enforcing incremental deformation steps. As
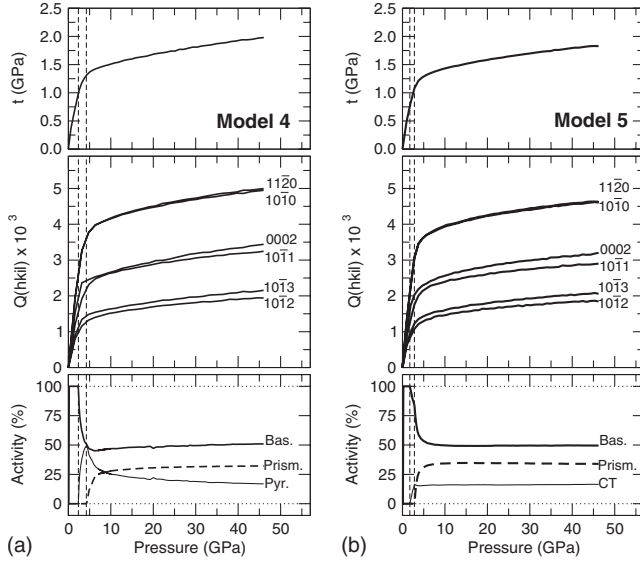
FIG. 6. Differential stress, lattice strain parameters, and relative activity of the deformation mechanisms as a function of pressure for simulations using models 4 and 5 in Table II. For model 4, vertical dashed lines at $P = 2.3$ GPa and $P = 4.3$ GPa correspond to the activation of pyramidal $\langle c+a \rangle$ and prismatic slip, respectively. For model 5, vertical dashed lines at $P = 1.7$ GPa and $P = 2.8$ GPa correspond to the activation of compressive twinning and prismatic slip, respectively.

deformation proceeds, crystals deform and rotate to generate preferred orientation. In VPSC calculations, the elastic response of the polycrystal is neglected, but grain rotations are properly accounted for, and this code has been used multiple times to model and understand textures obtained in DAC RDX experiments.[55]

A limitation of VPSC in connection with this work is that VPSC is based on an incompressible constitutive law, and calculations should be run at constant volume, that is with $(\epsilon_x + \epsilon_y + \epsilon_z) = 0$. According to the equation of state, volumetric strain imposed by compressing polycrystalline cobalt to a pressure of 46 GPa is 17%, corresponding to axial strains of 5.7%. In the actual sample, 5.7% of the applied axial strain $\epsilon_z^{0-K_S}$ is accommodated elastically and the remaining 11.3% plastically, increasing stress in the radial directions σ_x and σ_y. We ran the VPSC calculations with strains corresponding to the actual plastic deformation applied to the DAC sample, which is to a maximum axial strain of 10% while preserving $\epsilon_x + \epsilon_y = -\epsilon_z$.

We used the parameters of models 4 and 5 in Table II to model the development of texture in polycrystalline cobalt deformed in the DAC. Simulations were performed in 200 steps, starting with a randomly oriented sample of 1000 grains assuming an effective interaction between grains. A viscoplastic linear hardening Voce law was used. Activity of slip systems in all 1000 grains is evaluated in each of the steps and orientations are updated accordingly. From the orientation distribution of 1000 grains, inverse pole figures were calculated to illustrate crystal orientation patterns. All texture processing has been performed with the software Beartex.[53]

In both cases, we obtain a well defined texture with a maximum located near 0001, that is, with the basal planes

perpendicular to the compression direction [Figs. 3(c) and 3(d)]. After 10% strain, the inverse pole figures of the compression direction have a maximum of 2.20 and 2.22 multiples of a random distributions (m.r.d.) for VPSC calculations using models 4 and 5, respectively. Differences can be seen in the exact location of the maximum. In the experimental data, the texture component is evenly spread at about 15° of the c direction. Simulations using model 4 give a maximum at about 15° of the c direction and centered around $(10\bar{1}l)$ planes. For model 5, this maximum is located at about 15° of the c direction and centered around $(11\bar{2}l)$ planes.

It should be noted that the 15° shift of the c direction in the inverse pole figure cannot be attributed to experimental errors and is clearly visible in the measured variations in diffraction intensities with orientation (e.g., Fig. 3 in Ref. 22). It is also well reproduced by VPSC calculations. It should also be noted that textures measured in hcp-Fe do not always show a full alignment of the c axes with the compression direction[69,70] and that a shift of the maximum from the c direction has been observed in hcp-Fe.[70]

The conclusion of this calculation is that, although the VPSC predicted textures were obtained by enforcing only the plastic component of strain, they show that both pyramidal $\langle c+a \rangle$ slip and compressive twinning activity are consistent with the texture measured experimentally in the DAC for Co.

IV. DISCUSSION

A. Validity of lattice strain parameters Q

In Sec. II C 3 we assumed that the experimental data could be adjusted to Eq. (15). This implies that the d spacings measured at $\psi = 54.7°$, $d_P(hkil)$, correspond to those associated with the hydrostatic pressure, and that the effect of differential stress can be summarized in the form of one unique lattice strain parameter Q.

Experimental data indicate that equation of states measured on stressed samples at $\psi = 54.7°$ do agree with those measured under quasihydrostatic conditions. Results of EPSC calculations support this observation as the hydrostatic strains adjusted to Eq. (15) do not depend significantly on the combination of activated plastic deformation mechanisms. In our models, small deviations can be observed between the calculated hydrostatic strains and those expected from the single-crystal elastic moduli, e.g., 0002 and $10\bar{1}3$ in Fig. 4, but those are significantly lower than typical errors due to differential stress. Therefore, our model supports the idea that equation of states measurements at $\psi = 54.7°$ on stressed samples are a valid alternative if no better solution for reducing the deviatoric stress can be found.

The assumption that the measured d spacings vary linearly with $(1 - 3 \cos^2 \psi)$ and can be summarized with a single parameter Q is more questionable. In the case of Co, d spacings measured for $11\bar{2}0$ do not follow this relation. The use of the lattice strain parameters Q is useful to compare experimental data and output of EPSC models. However, the model predictions should be compared against actual measured d spacings, as shown in Fig. 1. In this figure we dem-

onstrate that both models 4 and 5 can correctly reproduce the essentially nonlinear experimental curves.

In the experimental data, we observe a split of lattice strains measured for 0002 and 0004 above 25 GPa (Fig. 2). This cannot be accounted for using the model presented here as strains calculated to 0002 will be equal to those calculated for 0004. This observation will have to be confirmed and modeled in further studies.

B. Average pressure and stress in the polycrystalline sample

It is interesting to note that the evolution of pressure with applied strain does not depend on the proposed plastic model (e.g., Fig. 5). Plastic deformation occurs at constant volume and is independent of pressure. As a consequence, it has no influence on the relation between the applied axial strain and the average pressure within the sample.

Axial stresses, on the other hand, show a very different behavior. At the highest compression, pure elastic compression results in an axial stress $\sigma_{33}=71.6$ GPa and radial stress $\sigma_{11}=\sigma_{22}=33.3$ GPa [Fig. 5(a)]. For optimized plastic models 4 and 5, we find $\sigma_{33}=47.5(1)$ GPa and $\sigma_{11}=\sigma_{22}=45.5(1)$ GPa.

Plastic deformation results in a redistribution of stress in the polycrystalline sample. Grains that deform plastically change the stress balance of the polycrystal, decreasing the average stress supported by the polycrystal in the axial direction while increasing the stress supported in the radial direction.

The evolution of differential stress with pressure is very similar for both optimized models (Fig. 6). In both cases, we find a fast increase in differential stress to 1.3 GPa at a pressure of 5 GPa. At 42.6 GPa, differential stress for models 4 and 5 are 2.0 and 1.8 GPa, respectively. The value of 1.3 GPa corresponds to stresses where all important deformation mechanisms are activated and could be qualified as yield strength for the present sample. Increase in differential stress between 1.3 and 1.9 GPa at higher pressures is related to a pressure-induced increase in elastic constants as well as strain hardening in the sample.

C. Strength and deformation mechanisms activities

Both optimized models 4 and 5 predict a very low strength and high activity of basal slip for hcp-Co, in line with observations under ambient pressure.[40,42] This is required to reproduce the observed relatively low lattice strains for pyramidal diffraction lines such as $10\bar{1}1$, $10\bar{1}2$, or $10\bar{1}3$. Lattice strains for those planes are extremely sensitive the values of the parameters τ_0 and θ_1 of the Voce hardening rule.

We also predict a relatively low strength and high activity for prismatic slip. This is required to match the observed lattice strains for $10\bar{1}0$ and $11\bar{2}0$. Prismatic slip is commonly observed in metals with the hcp structure and has been reported in Co.[44] The lattice strains above are extremely sensitive to τ_0 and θ_1 for prismatic slip.

Models 4 and 5 differ in the activation of pyramidal $\langle c+a\rangle$ slip or compressive twinning, respectively. Compressive
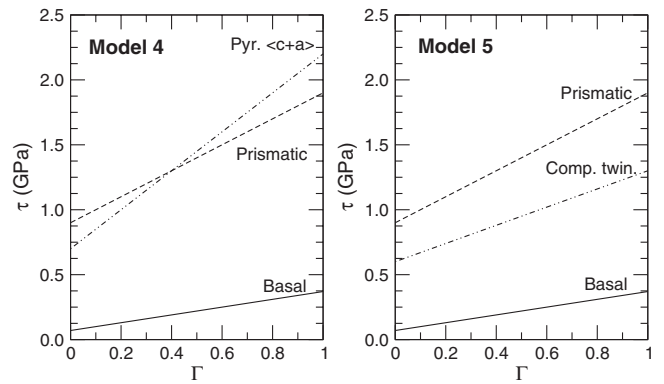

FIG. 7. Absolute CRSS of each active deformation mechanism as a function of accumulated plastic shear strain in the grain for models 4 and 5 in Table II.

twinning has been reported in cobalt in the literature,[40,43] whereas observations of pyramidal $\langle c+a\rangle$ slip are scarce. Experimentally measured textures show a maximum evenly spread at about 15° of the c direction. VPSC simulations using model 4 show a maximum at about 15° of the c direction and centered around $(10\bar{1}l)$ planes. For model 5, this maximum is located at about 15° of the c direction and centered around $(11\bar{2}l)$ planes. This suggests that a full model accounting for the plastic deformation of hcp-Co should probably include a combination of both pyramidal $\langle c+a\rangle$ and compressive twinning. In the future, we expect to be able to resolve this issue by repeating our simulations using an improved version of EPSC with slip and twin reorientation.

In both optimized simulations, activation of pyramidal $\langle c+a\rangle$ slip or compressive twinning controls lattice strains for the 0002 diffraction line. Voce law parameters were optimized to force activation of either $\langle c+a\rangle$ slip or compressive twinning before activation of prismatic slip. Large hardening coefficients were necessary for both mechanisms to ensure a later activation of prismatic slip. In all cases, activation of prismatic slip prior to pyramidal $\langle c+a\rangle$ slip or compressive twinning resulted in models that do not fit the experimental data.

Figure 7 presents the absolute CRSS of each active deformation parameter as a function of accumulated plastic shear strain in the grain Γ for models 4 and 5 in Table II. For basal slip, Γ can reach values as high as 4 in some grains at the end of the simulation. For other deformations modes, final values of Γ range between 0.8 and 2, depending on grains and deformation mechanisms. The hardening law we used does not account for an effect of pressure on the CRSS and all experimental data could be fit using the simple, linear, strain dependent hardening law shown in Fig. 7. More experiments, where plastic deformation of the sample starts later in the compression rather than ambient pressure, will be required to quantify an effect of pressure on plasticity, but we could not extract such information from the present data.

D. Stress heterogeneities within the polycrystal

Figure 6 presents the evolution of the average differential stress as a function of pressure for models 4 and 5 while Fig.
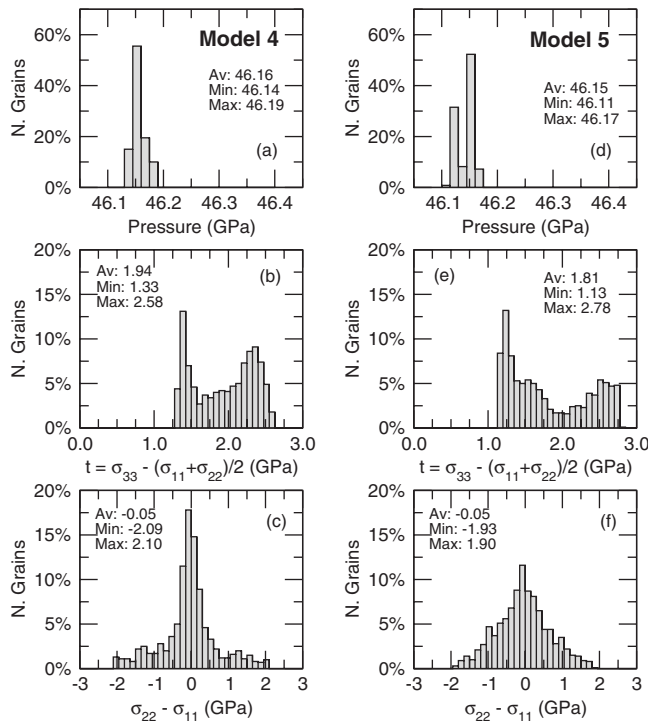
FIG. 8. Histograms of the distribution of pressure, differential stress, and lateral stress among grains in the sample at P =46.2 GPa for EPSC calculations using models 4 [(a),(b),(c)] and 5 [(d),(e),(f)] in Table II.

8 shows histograms of the distribution of pressure, differential stress $t = \sigma_{33} - (\sigma_{11} + \sigma_{22})$, and lateral stress $(\sigma_{22} - \sigma_{11})$ among grains in the sample at the end of compression for both models. Pressure is very uniform and only varies by 0.05 GPa from grain to grain, which is on the order of magnitude of numerical errors in the calculation. Distributions of differential and lateral stress, however, are not uniform and model dependent.

Lateral stresses show a distribution centered around 0 GPa, as expected. For both models, minimum and maximum lateral stresses among grains are of the same order of magnitude than the average differential stress in the sample.

For both models, differential stress among grains shows a bimodal distribution whose mean corresponds to the average differential stress in the polycrystalline sample. Differences between the minimum and maximum stress among grains is lower than the average differential stress but well over 1 GPa. Two grain families can be identified: grains in soft orientations that were submitted to large plastic deformation and show a relatively low differential stress, and grains in hard orientations that were submitted to less plastic deformation and show a relatively high differential stress.

The relevant conclusion of the stress distribution analysis is that plasticity leads to a significant spread of stress among grains. This explains why models based on assuming uniform states in the aggregate[14] yield inconsistent stresses and elastic constants for materials deforming plastically.[21,22,32,33] Figure 8 demonstrates that, as slip or twinning is activated inside a grain, deviatoric stresses are relaxed within the grain, and the state of stress among grains in the aggregate

becomes very heterogeneous. This cannot be accounted for with theories relying solely on continuum mechanisms and numerical models such as those presented here should be applied.

E. Limitations of the model

As demonstrated in this paper, EPSC models are very successful for understanding and modeling internal stress and strain in plastically deforming polycrystals. The current approach, however, has limitations. They can be separated in two categories: limitations of the self-consistent approach, and limitations of the actual code we used.

The self-consistent model treats each grain as an ellipsoidal elastoplastic inclusion embedded within a homogeneous elastoplastic effective medium. As such, local interactions from grain to grain and heterogeneities within the grains themselves are not accounted for. Three-dimensional (3D) full-field polycrystalline models can predict local-field variations.[71–73] These calculations show important heterogeneities within grains and a strong localization of stress and strain near the grain boundaries. However, the precision of those models comes with large computational cost and complexity, and they cannot be systematically applied for interpreting experimental results. Mean-field approaches such as EPSC models are very successful and currently remain most convenient to explore and understand experimental results.[73]

The EPSC code we used did not account for grain reorientation associated with slip and twinning deformation. While we do not expect that texture evolution will change the qualitative conclusions of this paper concerning the type and role of deformation mechanisms, we do expect that it will influence CRSS and hardening parameters. In the current version of the model, grains that have an orientation favorable for the activation of a deformation mechanism will be activated at each step. In reality, those grains should rotate and finally reach orientations less favorable for the deformation mechanism. As such, we expect the hardening parameters reported in Table II to be slightly overestimated.

V. CONCLUSIONS

A modification of the EPSC model of Turner and Tomé[31] was used to successfully model x-ray diffractions measurements performed on hcp-Co samples plastically deformed under high pressure. Important information provided by the model includes: actual values of differential stress in the polycrystal, stress distribution among grains in the sample, as well as identification, relative activity, and strength of the active deformation mechanisms.

The model confirms that the effect of differential stress and plastic deformation on measured d spacings is often minimal at $\psi = 54.7°$. Therefore, measurements of d spacings at this angle can be used to estimate hydrostatic equation of states if no better solution is available. This is particularly applicable to measurements above 100 GPa for which no hydrostatic pressure transmitting medium is available.

We find that the plastic behavior of hcp-Co plastically deformed under high pressure is controlled by basal and pris-

matic slip of $\langle a \rangle$ dislocations, and either pyramidal slip of $\langle c+a \rangle$ dislocations or compressive twinning. Strength and hardening coefficients for those mechanisms have been determined and are listed in Table II. Basal slip is by far the easiest and most active deformation mechanism, with an initial strength of 0.07 GPa and a linear hardening coefficient of 0.30 GPa.

For hcp-Co deformed axially in the diamond-anvil cell, we observe a fast increase in differential stress to 1.3 GPa between pressures of 0 and 5 GPa. The later part of the compression shows a slower increase in differential stress with pressure. At 42 GPa, the differential stress in hcp-Co is 1.9 ± 0.1 GPa. The transition between the fast and slow increase in differential stress in the sample is related to the sequential activation of plastic deformation mechanisms in the sample.

EPSC models are very powerful and overcome many limitations of models based on continuum elasticity theory for the interpretation of x-ray diffraction data measured on stressed samples. They should be used for the interpretation of all high pressure deformation experiments where x-ray diffraction is used to probe stress within a polycrystalline sample.

*sebastien.merkel@univ-lille1.fr

[1] S. Klotz, M. Braden, and J. M. Besson, Phys. Rev. Lett. **81**, 1239 (1998).

[2] F. Occelli, D. L. Farber, J. Badro, C. M. Aracne, D. M. Teter, M. Hanfland, B. Canny, and B. Couzinet, Phys. Rev. Lett. **93**, 095502 (2004).

[3] A. F. Goncharov, J. Crowhurst, and J. M. Zaug, Phys. Rev. Lett. **92**, 115502 (2004).

[4] M. B. Weinberger, S. H. Tolbert, and A. Kavner, Phys. Rev. Lett. **100**, 045506 (2008).

[5] G. Steinle-Neumann, L. Stixrude, and R. E. Cohen, Phys. Rev. B **60**, 791 (1999).

[6] X. Sha and R. E. Cohen, Phys. Rev. B **74**, 064103 (2006).

[7] L. Vočadlo, Earth Planet. Sci. Lett. **254**, 227 (2007).

[8] G. Steinle-Neumann, Phys. Rev. B **77**, 104109 (2008).

[9] Y. Ma, M. Somayazulu, G. Shen, H. Mao, J. Shu, and R. Hemley, Phys. Earth Planet. Inter. **143-144**, 455 (2004).

[10] R. J. Hemley, H. K. Mao, G. Shen, J. Badro, P. Gillet, M. Hanfland, and D. Häusermann, Science **276**, 1242 (1997).

[11] D. Yamazaki and S.-I. Karato, Rev. Sci. Instrum. **72**, 4207 (2001).

[12] S. Merkel, H. R. Wenk, J. Shu, G. Shen, P. Gillet, H. K. Mao, and R. J. Hemley, J. Geophys. Res. **107**, 2271 (2002).

[13] Y. Wang, W. B. Duhram, I. C. Getting, and D. J. Weidner, Rev. Sci. Instrum. **74**, 3002 (2003).

[14] A. K. Singh, C. Balasingh, H. K. Mao, R. J. Hemley, and J. Shu, J. Appl. Phys. **83**, 7567 (1998).

[15] A. K. Singh, H. K. Mao, J. Shu, and R. J. Hemley, Phys. Rev. Lett. **80**, 2157 (1998).

[16] H. K. Mao, J. Shu, G. Shen, R. J. Hemley, B. Li, and A. K. Singh, Nature (London) **396**, 741 (1998); **399**, 280 (1999).

[17] S. Merkel, J. Shu, P. Gillet, H. Mao, and R. Hemley, J. Geophys. Res. **110**, B05201 (2005).

[18] W. L. Mao *et al.*, J. Geophys. Res. **113**, B09213 (2008).

[19] D. Antonangeli, M. Krisch, G. Fiquet, D. L. Farber, C. M. Aracne, J. Badro, F. Occelli, and H. Requardt, Phys. Rev. Lett. **93**, 215505 (2004).

[20] D. Antonangeli, M. Krisch, G. Fiquet, J. Badro, D. L. Farber, A. Bossak, and S. Merkel, Phys. Rev. B **72**, 134303 (2005).

[21] D. Antonangeli, S. Merkel, and D. L. Farber, Geophys. Res. Lett. **33**, L24303 (2006).

[22] S. Merkel, N. Miyajima, D. Antonangeli, G. Fiquet, and T. Yagi, J. Appl. Phys. **100**, 023510 (2006).

[23] J. C. Crowhurst, D. Antonangeli, J. M. Brown, A. F. Goncharov, D. L. Farber, and C. M. Aracne, Appl. Phys. Lett. **89**, 111920 (2006).

[24] I. Noyan and J. Cohen, *Residual Stress: Measurements by Diffraction and Interpretation* (Springer-Verlag, New York, 1987).

[25] M. R. Daymond, Rev. Mineral. Geochem. **63**, 427 (2006).

[26] B. Clausen, T. Lorentzen, and T. Leffers, Acta Mater. **46**, 3087 (1998).

[27] M. R. Daymond, M. A. M. Bourke, and R. B. Von Dreele, J. Appl. Phys. **85**, 739 (1999).

[28] P. Dawson, D. Boyce, S. MacEwen, and R. Rogge, Mater. Sci. Eng., A **313**, 123 (2001).

[29] M. R. Daymond and N. W. Bonner, Mater. Sci. Eng., A **340**, 272 (2003).

[30] D. Brown, M. Bourke, B. Clausen, T. Holden, C. Tome, and R. Varma, Metall. Mater. Trans. A **34**, 1439 (2003).

[31] P. A. Turner and C. N. Tomé, Acta Metall. Mater. **42**, 4143 (1994).

[32] D. J. Weidner, L. Li, M. Davis, and J. Chen, Geophys. Res. Lett. **31**, L06621 (2004).

[33] L. Li, D. J. Weidner, J. Chen, M. T. Vaughan, M. Davis, and W. B. Durham, J. Appl. Phys. **95**, 8357 (2004).

[34] P. C. Burnley and D. Zhang, J. Phys.: Condens. Matter **20**, 285201 (2008).

[35] C. S. Yoo, H. Cynn, P. Söderlind, and V. Iota, Phys. Rev. Lett. **84**, 4132 (2000).

[36] H. Fujihisa and K. Takemura, Phys. Rev. B **54**, 5 (1996).

[37] D. Antonangeli, L. R. Benedetti, D. L. Farber, G. Steinle-Neumann, A. Auzende, J. Badro, M. Hanfland, and M. Krisch, Appl. Phys. Lett. **92**, 111911 (2008).

[38] H. J. McSkimin, J. Appl. Phys. **26**, 406 (1955).

[39] D. Antonangeli, M. Krisch, D. L. Farber, D. G. Ruddle, and G. Fiquet, Phys. Rev. Lett. **100**, 085501 (2008).

[40] A. Seeger, H. Kronmüller, O. Boser, and M. Rapp, Phys. Status Solidi **3**, 1107 (1963) b.

[41] M. H. Yoo and C. T. Wei, J. Appl. Phys. **38**, 4317 (1967).

[42] H. M. Theiringer, Z. Metallkd. **59**, 476 (1968).

[43] S. Vaidya and S. Mahajan, Acta Metall. **28**, 1123 (1980).

[44] X. Wu, N. Tao, Y. Hong, G. Liu, B. Xu, J. Lu, and K. Lu, Acta Mater. **53**, 681 (2005).

[45] A. A. Karimpoor, U. Erb, K. T. Aust, and G. Palumbo, Scr. Mater. **49**, 651 (2003).

[46] X. Zhang and C. Jia, Mater. Sci. Eng., A **418**, 77 (2006).

[47] G. Zheng, Y. Wang, and M. Li, Acta Mater. **53**, 3893 (2005).

[48] T. H. K. Barron and M. L. Klein, Proc. Phys. Soc. London **85**, 523 (1965).

[49] D. C. Wallace, Solid State Phys. **25**, 301 (1970).

[50] D. C. Wallace, *Thermodynamics of Crystals* (Wiley, New York, 1972).

[51] U. F. Kocks, C. Tomé, and H. R. Wenk, *Texture and Anisotropy: Preferred Orientations and their Effects on Material Properties* (Cambridge University Press, Cambridge, 1998).

[52] S. Matthies and G. W. Vinel, Phys. Status Solidi B **112**, K111 (1982).

[53] H. R. Wenk, S. Matthies, J. Donovan, and D. Chateigner, J. Appl. Crystallogr. **31**, 262 (1998).

[54] L. Lutterotti, S. Matthies, and H. R. Wenk, IUCR: Newsl. of the CPD **21**, 14 (1999).

[55] H. R. Wenk, I. Lonardelli, S. Merkel, L. Miyagi, J. Pehl, S. Speziale, and C. E. Tommaseo, J. Phys.: Condens. Matter **18**, S933 (2006).

[56] S. Matthies, H. G. Priesmeyer, and M. R. Daymond, J. Appl. Crystallogr. **34**, 585 (2001).

[57] S. Matthies, S. Merkel, H. R. Wenk, R. J. Hemley, and H. K. Mao, Earth Planet. Sci. Lett. **194**, 201 (2001).

[58] S. Merkel and T. Yagi, J. Phys. Chem. Solids **67**, 2119 (2006).

[59] S. R. Agnew, C. N. Tomé, D. W. Brown, T. M. Holden, and S. C. Vogel, Scr. Mater. **48**, 1003 (2003).

[60] S. Agnew, D. Brown, and C. Tomé, Acta Mater. **54**, 4841 (2006).

[61] R. Hill, J. Mech. Phys. Solids **13**, 89 (1965).

[62] J. W. Hutchinson, Proc. R. Soc. London, Ser. A **319**, 247 (1970).

[63] S. Merkel and T. Yagi, Rev. Sci. Instrum. **76**, 046109 (2005).

[64] T. S. Duffy, G. Shen, D. L. Heinz, J. Shu, Y. Ma, H. K. Mao, R. J. Hemley, and A. K. Singh, Phys. Rev. B **60**, 15063 (1999).

[65] A. Kavner and T. S. Duffy, Phys. Rev. B **68**, 144101 (2003).

[66] S. Speziale, S. R. Shieh, and T. S. Duffy, J. Geophys. Res. **111**, B02203 (2006).

[67] A. Kavner, J. Geophys. Res. **112**, B12207 (2007).

[68] R. A. Lebensohn and C. N. Tomé, Mater. Sci. Eng., A **175**, 71 (1994).

[69] H. R. Wenk, S. Matthies, R. J. Hemley, H. K. Mao, and J. Shu, Nature (London) **405**, 1044 (2000).

[70] S. Merkel, H. R. Wenk, P. Gillet, H. K. Mao, and R. J. Hemley, Phys. Earth Planet. Inter. **145**, 239 (2004).

[71] H. Moulinec and P. Suquet, Comput. Methods Appl. Mech. Eng. **157**, 69 (1998).

[72] R. A. Lebensohn, Acta Mater. **49**, 2723 (2001).

[73] O. Castelnau, D. K. Blackman, R. A. Lebensohn, and P. Ponte Castañeda, J. Geophys. Res. **113**, B09202 (2008).